Optical signatures of radiation belt electron precipitation induced by ground-based VLF transmitters

R. A. Marshall,[1] R. T. Newsome,[2] N. G. Lehtinen,[2] N. Lavassar,[2] and U. S. Inan[2]

Received 23 February 2010; revised 1 April 2010; accepted 14 April 2010; published 7 August 2010.

[1] Numerical simulations are presented of optical emissions in the ionosphere due to electron precipitation caused by ground-based VLF transmitters. Ray tracing and precipitation calculations are made to estimate the flux precipitated from the inner magnetosphere for existing ground-based VLF transmitters as well as hypothetical transmitters with controlled parameters. The resulting precipitated fluxes are used to estimate ionization profiles through Monte Carlo simulations, and the ionization profiles are converted to photon volume emission rates. The results are extended over a range of L shells and longitudes. Results show that the NWC transmitter at North West Cape, Australia, creates the strongest optical signature because of its high power, latitude of ~35°, and low frequency. The resulting optical signal has a peak of <0.1 R; however, we calculate that this should be detectable using sensitive photometric instruments and controlled modulation experiments.

Citation: Marshall, R. A., R. T. Newsome, N. G. Lehtinen, N. Lavassar, and U. S. Inan (2010), Optical signatures of radiation belt electron precipitation induced by ground-based VLF transmitters, *J. Geophys. Res.*, *115*, A08206, doi:10.1029/2010JA015394.

1. Introduction

[2] Trapped energetic electrons in the Earth's radiation belts are affected by resonance interactions with VLF (3–30 kHz) whistler mode waves, which can cause them to be scattered into the loss cone. While sources of VLF whistler waves include naturally occurring chorus, hiss, and lightning discharges, *Abel and Thorne* [1998] were the first to show that ground-based transmitters could have a significant effect on >100 keV electron populations, albeit for $L < 2.6$.

[3] There are at least three experimental methods for measuring electron precipitation from VLF transmitters. First, satellites such as SAMPEX [e.g., *Baker et al.*, 1993] can make direct measurements of radiation belt pitch angle distributions and can measure the population of electrons in the bounce and drift loss cones. A clear example of such a measurement was made by *Sauvaud et al.* [2008] using data from the DEMETER satellite [*Parrot*, 2006]. However, satellite measurements are necessarily transient, and the precipitation signature from VLF transmitters may be small enough to require long-period averaging [*Inan et al.*, 2007]. Second, subionospheric VLF probing techniques [*Inan et al.*, 2007] can detect changes in the *D* region ionospheric density and by controlled experiments can be correlated to the VLF transmitter signal; this is the same principle as lightning-induced electron precipitation (LEP), which is regularly observed via this subionospheric VLF technique [*Helliwell et al.*, 1973; *Peter and Inan*, 2007, and references therein]. However, a potential issue with the subionospheric VLF technique is that the transmitter may directly heat the overlying ionosphere, and the VLF technique cannot distinguish between this heating and the expected precipitation signature that is the aim of the experiment. It has been suggested that this may affect the results of *Inan et al.* [2007]; current experiments are aimed at detecting the effect in the conjugate region, which will not be affected by transmitter heating.

[4] The third possible measurement technique is optical detection from ground-based instruments. While the VLF transmitter signal may heat the ionosphere, it is not intense enough to directly excite optical emissions. If we assume that the VLF transmitter radiates isotropically (an upper limit since VLF transmitters primarily radiate laterally) and that the ionosphere at 100 km is in the far field (~7λ for a 20 kHz transmitter), the electric field amplitude due to a 1 MW transmitter is only ~80 mV m^{-1}; ionization requires a minimum of ~10 V m^{-1} in the ionosphere [e.g., *Moss et al.*, 2006]. However, electrons precipitating due to pitch angle scattering by the transmitter will excite optical emissions. Sensitive ground-based instruments may be able to detect this signal with carefully designed experiments; space-borne optical instruments will again suffer from transient coverage of the affected area, just like space-borne particle detectors. In this paper, we calculate the expected optical emission rates and intensities for existing ground-based transmitters to determine whether or not precipitation from ground-based transmitters is observable via optical methods. Furthermore,

[1]Center for Space Physics, Boston University, Boston, Massachusetts, USA.
[2]Space, Telecommunications, and Radioscience Laboratory, Stanford University, Stanford, California, USA.

0148-0227/10/2010JA015394

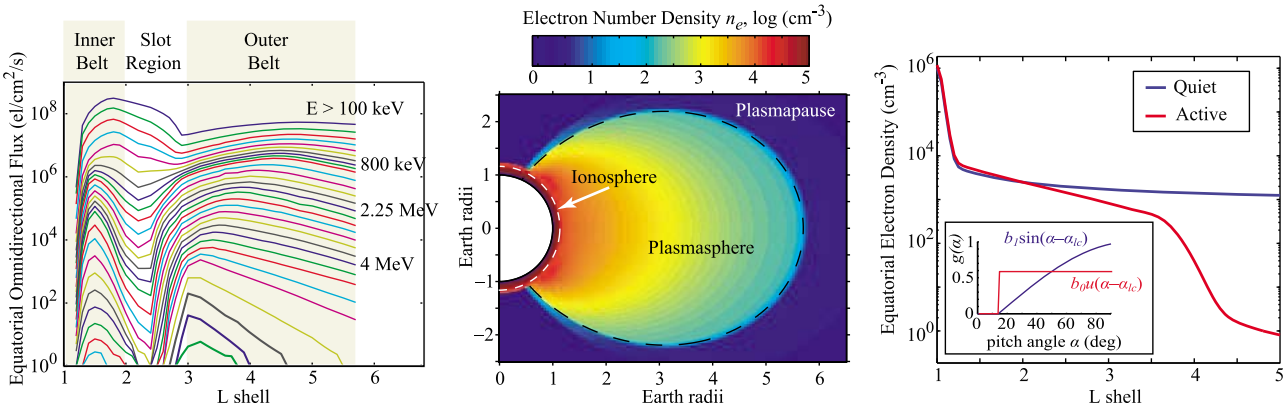

Figure 1. (left) Equatorial energetic electron flux as a function of L shell. Each curve gives the particle flux for electrons with energies above the given threshold. (middle) Cold plasmasphere density in a 2-D slice for quiet conditions, with L_{pp} = 5.5 (where L_{pp} is the L value location of the plasmapause). (right) Slice of plasmasphere density along magnetic equator for the quiet (Kp_{max} = 0, L_{pp} = 5.5) and active (Kp_{max} = 4, L_{pp} = 3.8) cases (where Kp_{max} is the maximum value of the magnetic index Kp over the past 24 h), as defined by the *Carpenter and Anderson* [1992] model. The inset shows the two different pitch angle distributions used in this paper.

we make similar calculations for hypothetical transmitters in order to investigate the effects of power, latitude, and frequency.

2. Methodology

[5] In this paper, we ultimately seek an estimate of the photon volume emission rates (photons cm^{-3} s^{-1}) in a number of predominant emission lines and bands, which are then integrated to ground-based or space-based camera views to yield brightness estimates in rayleighs in order to compare with potential camera or photometer measurements. There are four sequential steps involved in this calculation: (1) ray tracing of the VLF transmitter signal through the plasmasphere and calculation of the interaction of these waves with radiation belt electrons, (2) a calculation, using a Monte Carlo model, of the resulting energy deposition as a function of altitude, (3) conversion of this energy deposition to ionization production and photon volume emission rates, and (4) a geometric calculation of the Rayleigh intensity that would be observed by a camera. We briefly discuss each of these calculations in sections 2.1–2.4, showing example outputs for the NWC transmitter at North West Cape, Australia.

2.1. Ray Tracing and Wave-Particle Interactions

[6] We use the model described by *Kulkarni et al.* [2008] to determine the electron fluxes precipitated from the radiation belts for a given transmitter. This model takes as inputs a radiation belt density and pitch angle distribution along with a plasmasphere (i.e., cold plasma) distribution. The radiation belt and plasmaspheric densities used are identical to those of *Bortnik et al.* [2006a] and are shown in Figure 1. The equatorial plasmasphere density is shown for both a quiet and a disturbed plasmasphere, which are compared in this paper.

[7] A ground-based transmitter is parameterized by geomagnetic latitude, transmitted power, and frequency. In this paper, as in work by *Kulkarni et al.* [2008], we use existing transmitters as well as hypothetical transmitters in order to investigate the effects of individual transmitter parameters. The model uses a 2-D ray tracing code [*Inan and Bell*, 1977] to propagate waves from the base of the ionosphere into the magnetosphere. The 2-D nature of the model does not allow for wave propagation across field lines in longitude; however, 3-D modeling has shown that such longitudinal propagation is negligible [*Cairó and Lefeuvre*, 1986]. The model then uses the method of *Bortnik et al.* [2006a] to determine the energetic electron precipitation signatures on the basis of pitch angle and energy scattering of the energetic radiation belt electrons. We refer to these two model components together as the Wave Induced Particle Precipitation (WIPP) code. Note that this model assumes a dipole radiation pattern for the VLF transmitter and accounts for attenuation of the waves as they propagate through the ionosphere according to *Helliwell* [1965, Figure 3-35] as well as Landau damping in the magnetosphere.

[8] Waves are injected over a series of L shells, and, in turn, precipitation signatures are given over a range of L shells as fluxes in units of electrons keV^{-1} cm^{-2} s^{-1} over energies from 30 eV to 7 MeV. In addition, pitch angle scattering is reported as $\Delta\alpha$ as a function of energy. The resulting precipitation signatures are scaled in longitude using the function given by *Bortnik et al.* [2006b, equation (1) and Figure 6]. This function accounts for the spread of power in the Earth-ionosphere waveguide before injection through the ionosphere.

2.2. Monte Carlo Model of Energy Deposition

[9] This precipitating flux from the WIPP model is converted to a distribution of electrons according to the following calculation: given the initial pitch angle distribution, the change in pitch angle $\Delta\alpha$, and the energy distribution, a large test population of electrons is generated, each with random momentum components but regulated such that the sum of all the electrons' energies equals the total energy in

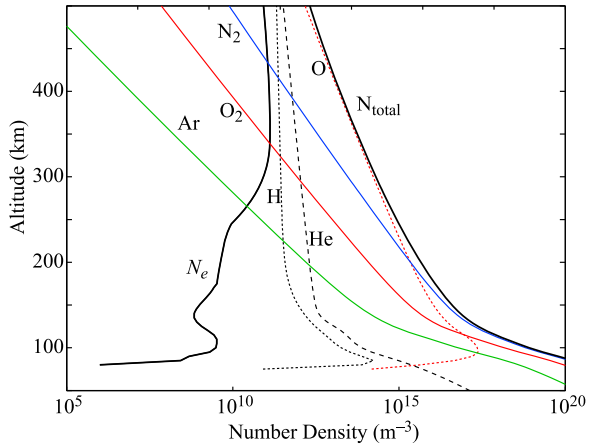

Figure 2. Ionospheric electron density and atmospheric constituents as a function of altitude, from the MSIS-E-90 model at nighttime, equatorial latitudes.

the precipitating flux. The electron momentum components are next input into a Monte Carlo model, presented by *Lehtinen et al.* [1999], of energy deposition in the upper atmosphere, starting from 300 km altitude and extending to the ground. In this model the electron motion is described by the Langevin equation, including elastic and inelastic scattering of electrons. Energy losses by excitation and ionization processes are described by the dynamic friction function [*Bethe and Ashkin*, 1953, p. 254]. The model uses the MSIS-E-90 model for nighttime equatorial atmospheric profiles, shown in Figure 2. We then compute the energy deposited, in eV m^{-3} s^{-1}, as a function of altitude.

[10] A problem exists with the Monte Carlo model in its current implementation, which has to do with the lowest energy electrons with $E < 2$ keV. The algorithm for the dynamic friction function assumes a minimum energy of 2 keV for primary electrons and so cannot properly calculate ionization due to electrons with energies below this minimum. The implications of this limitation are discussed in section 3.2 and Figure 7.

2.3. Ionization and Optical Excitation Rates

[11] From the Monte Carlo simulation of energy deposition, the rate of new ionization production follows, in pairs m^{-3} s^{-1}, as a function of altitude, assuming the well-known empirical result that each 35.5 eV produces one ion-electron pair. The ionization rates are then taken with the MSIS-E-90 atmospheric model and the international reference ionosphere model of ionospheric density to compute optical excitation (and thus emission) rates for a number of optical emission systems and lines. In particular, we calculate N_2 first positive (1 P; $B^3\Pi_g \rightarrow A^3\Sigma_u^+$), N_2 second positive (2 P; $C^3\Pi_u \rightarrow B^3\Pi_g$), N_2 Vegard-Kaplan (VK; $A^3\Sigma_u^+ \rightarrow X^1\Sigma_g^+$), N_2^+ first negative (1 N; $B^2\Sigma_u^+ \rightarrow X^2\Sigma_g^+$), N_2^+ Meinel (M; $A^2\Pi \rightarrow X^2\Sigma_g^+$), O_2^+ first negative (1 N; $b^4\Sigma_g^- \rightarrow a^4\Pi_u$), O($^1S$) green line (557.7 nm; $2p^4\ ^1D \rightarrow 2p^4\ ^1S$), and O($^1D$) red line (630.0 nm; $2p^4\ ^3P \rightarrow 2p^4\ ^1D$).

[12] Optical emissions in photons m^{-3} s^{-1} are calculated from the ionization rate above, as a function of altitude, by the method used by *Bell et al.* [1995] and *Lehtinen et al.* [1997, 1999]. This method uses a generic cross section given by *Vallance Jones* [1974, p. 92]:

$$\sigma(E) = \frac{\sigma_{\max} E_{\max}^2 (E - I)}{E[E_{\max}(E_{\max} - 2I) + EI]}, \tag{1}$$

where $\sigma_{\max}$ is the maximum cross section, $E_{\max}$ is the energy at which that maximum is attained, and I is the ionization potential; here $\sigma_{\max}$ and $E_{\max}$ are taken from *Vallance Jones* [1974], and I is taken from *Rees* [1992]. The numerical values of these three parameters are given in Table 1. The production rates of individual ions and excited states are then calculated from the total ionization cross section using equations (4.2.1f)–(4.2.1l) of *Vallance Jones* [1974, p. 105]. Finally, emission rates (γ) in units of photons m^{-3} s^{-1} are calculated according to the following relations, including quenching and cascading from higher states [*Vallance Jones*, 1974, p. 119]:

$$\gamma_{N_2 1\,P} = \frac{a_{N_2 C}\, r_{N_2 C}}{a_{N_2 C} + \alpha_{N_2 C,\mathrm{air}}(N_{N_2} + N_{O_2})}, \tag{2a}$$

$$\gamma_{N_2 1\,P} = a_{N_2 B} \frac{r_{N_2 B} + \gamma_{N_2 2\,P}}{a_{N_2 B} + \alpha_{N_2 B,\mathrm{air}}(N_{N_2} + N_{O_2})}, \tag{2b}$$

$$\gamma_{N_2 VK} = a_{N_2 A} \frac{r_{N_2 A} + \gamma_{N_2 1\,P}}{a_{N_2 A} + \alpha_{N_2 A,O} N_O}, \tag{2c}$$

$$\gamma_{N_2^+ M} = \frac{a_{N_2^+ A}\, r_{N_2^+ A}}{a_{N_2^+ A} + \alpha_{N_2^+ A,\mathrm{air}}(N_{N_2} + N_{O_2})}, \tag{2d}$$

$$\gamma_{N_2^+ 1\,N} = \frac{a_{N_2^+ B}\, r_{N_2^+ B}}{a_{N_2^+ B} + \alpha_{N_2^+ B,\mathrm{air}}(N_{N_2} + N_{O_2})}, \tag{2e}$$

$$\gamma_{O_2^+ 1\,N} = \frac{a_{O_2^+ b}\, r_{O_2^+ b}}{a_{O_2^+ b} + \alpha_{O_2^+ b,N_2} N_{N_2}}, \tag{2f}$$

$$\gamma_{O^1 S} = a_{O^1 S} \frac{r_{O^1 S} + \alpha_{N_2 A,O} N_{N_2 A} N_O}{a_{O^1 S} + \alpha_{O^1 S,O_2} N_{O_2} + \alpha_{O^1 S,O} N_O}, \tag{2g}$$

$$\gamma_{O^1 D} = a_{O^1 D} \frac{r_{O^1 D} + \gamma_{O^1 S}}{a_{O^1 D} + \alpha_{O^1 D,N_2} N_{N_2}}, \tag{2h}$$

Table 1. Ionization Potential, Maximum Cross Section, and Maximum Energy, Relating to Equation (1), for Given States[a]

State	I (eV)	$E_{\max}/E_{re}$[b]	$\sigma_{\max}$ (cm^2)
O_2	12.2	100	0.27×10^{-15}
N_2	15.6	100	0.24×10^{-15}
N_2A	6.0	10	0.28×10^{-16}
N_2B	7.3	12	0.11×10^{-15}
N_2C	11.0	16	0.38×10^{-16}
O	13.6	100	0.15×10^{-15}
O(S)	4.17	10	0.28×10^{-16}
O(D)	1.96	5.6	0.25×10^{-17}

[a] I, ionization potential; $\sigma_{\max}$, maximum cross section; $E_{\max}$, maximum energy.
[b] Electron rest energy, given by $m_e c^2/q_e = 0.511$ MeV.

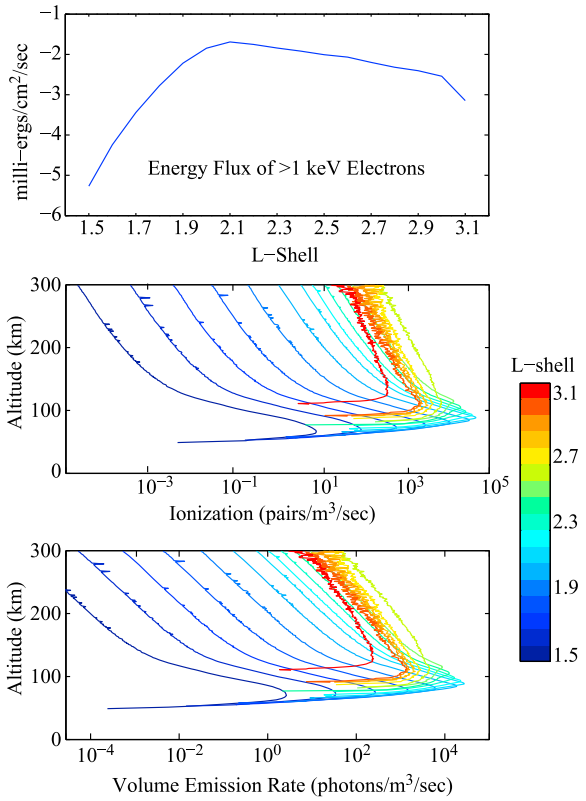

Figure 3. Results for the NWC transmitter at North West Cape, Australia, for a quiet plasmasphere and square pitch angle distribution. (top) Precipitated flux versus L of electrons with $E > 1$ keV. (middle) Ionization produced at each L location as a function of altitude. (bottom) Same as Figure 3 (middle) but for optical emissions, N_2 1 P bands.

where a is the rate constant and $\alpha_{X,Y}$ is the quenching rate constant of X by collisions with Y, both taken from *Vallance Jones* [1974, p. 119]. The r values are the ionization and excitation rates from section 2.2, and the N values are the neutral densities, taken from the MSIS-E-90 model.

[13] Figure 3 shows an example calculation for the NWC transmitter located at North West Cape, Australia. As shown by *Kulkarni et al.* [2008] and as we will show, the NWC transmitter is the most effective among existing transmitters at causing precipitation. Figure 3 (top) shows the precipitated flux in energy units for electrons with energies greater than 1 keV (we will show in section 3.2 that electrons with energies below 1 keV do not contribute significantly to the energy flux). Figure 3 (middle) shows the output of the Monte Carlo code, i.e., the ionization produced at each L shell as a function of altitude. The resulting optical emission rates in the N_2 first positive band system are shown in Figure 3 (bottom). In section 3 we showsimilar optical emission rate calculations for other existing transmitters.

[14] The "noisy" nature of the profiles at high L shells, as well as the random spikes at high altitudes in the low L shell profiles, is due to the finite statistics of the Monte Carlo code. In our simulations we use 10,000 test electrons to create these profiles, and only a small number of electrons deposit appreciable energy at high altitudes. The use of more electrons (e.g., 1 million) would result in smoother profiles but at the expense of significant computational time.

[15] Figure 4 shows isosurface contours of the optical emission rates for the NWC transmitter, again for the N_2 1 P bands, plotted in geographic coordinates over a map of Australia. Figure 4 clearly demonstrates the tendency toward higher altitudes at higher latitudes or L shells due to the increase in low-energy precipitation at high L shells.

2.4. Integration to Camera View

[16] Given the photon volume emission rates in photons m^{-3} s^{-1} over a 3-D emitting region that covers a range of altitudes, L shells, and longitudes, we project this emitting volume to geographic coordinates and integrate through line of sight to a specified viewing location, either above the emitting volume (i.e., what might be seen by a satellite) or on the ground (where a ground-based instrument would observe). In this paper we only show one such example; later we will use the volume emission rates as a function of L shell to compare different outputs since the peak intensity in the integrated camera view scales linearly with the peak of the volume emission rate.

[17] Figure 5 shows views of the optical signature in rayleighs for both bird's-eye views (Figure 5, top) and ground-based camera views (Figure 5, bottom) for the NWC transmitter. Intensity maps are shown for the N_2 1 P, N_2^+ 1 N, O(^1S) 5577 Å, and O(^1D) 6300 Å emissions. The ground-based views cover 360° of azimuth and 50° of elevation angle from the ground. One can see that observing from Gingin, Western Australia, the intensity peaks at a location just west of south and at 10°–20° elevation angle, with peak intensity of ~50 mR, ~6 mR, ~15 mR, and ~0.5 mR for the four emissions in the order listed above and as shown in Figure 5. Note that these intensities do not include atmospheric extinction; this will be less prevalent in the red emissions but of considerable importance for the prevalent N_2^+ 1 N emission line at 4278 Å.

3. Model Results

[18] Section 2 demonstrated the results of each simulation step for the NWC transmitter. Note that the precipitated flux

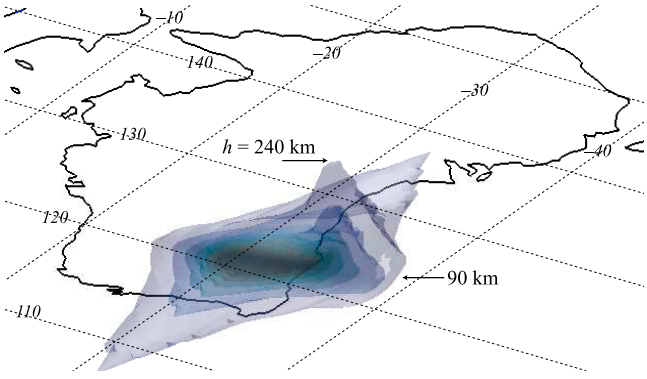

Figure 4. Isocontours of N_2 1 P emission rates over NWC. Optical emissions are present at higher altitudes for higher L shells (higher latitude). The magnetic declination at 40°S, 120°E is ~3°18′ west of north.

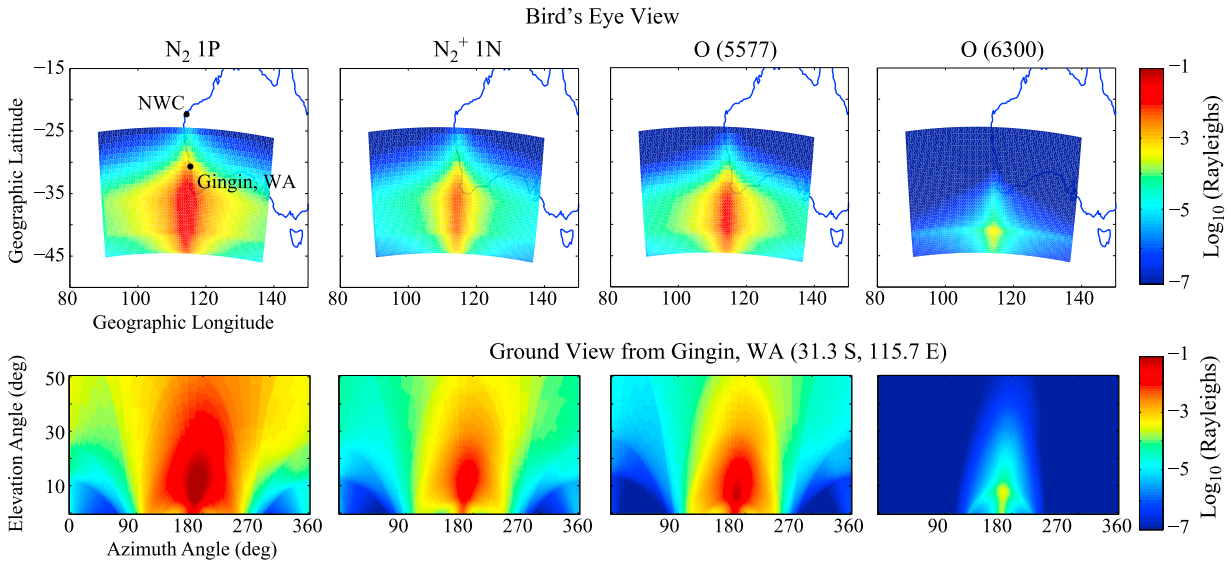

Figure 5. Camera views from (top) satellite and (bottom) ground-based camera at Gingin, Western Australia, of precipitation signatures from the NWC transmitter, with parameters as given in Table 2.

in section 2.1 is identical to that found by *Kulkarni et al.* [2008], except that in that work only electrons with energies $E > 100$ keV were considered. That work also conducted calculations of precipitated flux for a number of other ground-based transmitters. We will not repeat those results here; rather, we will restrict the results shown to the optical emission rates.

3.1. Existing VLF Transmitters

[19] Figure 5 shows the Rayleigh intensities in four optical bands and lines due to precipitation from the NWC transmitter. This calculation uses a square pitch angle distribution and a quiet plasmasphere. Note that the highest intensities are on the order of 6–50 mR in the N_2 1 P, N_2^+ 1 N, and O(^1S) emissions, while the O(^1D) emissions peak at about 0.5 mR. In section 4 we will discuss the implications of these results for experimental detection of these emissions.

[20] Table 2 lists the transmitter parameters for NWC and a variety of other known VLF transmitters around the globe. These are listed in ascending order of geomagnetic latitude; in fact, this list was chosen for the variety of latitudes, powers, and frequencies.

[21] Figure 6 compares the effectiveness of each of these transmitters through their volume emission rates. The values plotted are the maximum emission rates (in altitude; i.e., the peak of each curve in Figure 3 (middle)) along the magnetic meridians of the transmitters, where the emissions are the strongest (as seen in the satellite views of Figure 5). Figure 6 (top) shows results for a square pitch angle distribution, and Figure 6 (bottom) uses a sine pitch angle distribution (shown in Figure 1). These results show that the precipitated flux and, in turn, the ionization and optical emissions are reduced by 2 orders of magnitude with a sine pitch angle distribution. As such the results in Figure 5 using a square pitch angle distribution must be considered an upper limit.

[22] Figure 6 also shows that NWC is the most effective transmitter for causing precipitation; this was also concluded by *Kulkarni et al.* [2008]. Of interest, however, is that the transmitters with highest latitude (NAA, NLM, and DHO) have a peak in their emissions at high L shells. These peaks are due to a high flux of lower-energy electrons <100 keV, which were not considered in earlier work [e.g., *Kulkarni et al.*, 2008].

3.2. Theoretical VLF Transmitters

[23] To investigate the effects of relevant transmitter parameters, we conduct a series of simulations involving theoretical transmitters, with variations in (1) transmitter frequency, (2) latitude, and (3) transmitted power as well as two different pitch angle distributions and two different plasmasphere densities. Similar calculations using the WIPP code were conducted by *Kulkarni et al.* [2008], and results for precipitated flux are described therein. In the current paper, we conduct similar precipitation simulations and then proceed with the Monte Carlo and optical calculations described in section 2.

[24] However, a significant difference between the precipitation calculations of *Kulkarni et al.* [2008] and those herein is the inclusion of lower-energy electrons, i.e., those with $E < 100$ keV. These "low"-energy electrons deposit their energy at higher altitudes compared to >100 keV electrons, so they are not detectable by subionospheric VLF techniques. But they produce significant increases in ionization and thus optical emissions.

Table 2. VLF Transmitters Around the Globe Used in This Study in Ascending Order of Geomagnetic Latitude or L Shell

Call Sign	Frequency (kHz)	Power (kW)	Latitude	Longitude	Magnetic Latitude (λ)	L Shell
NPM	21.4	424	21.42	201.85	21.26	1.17
NAU	40.75	100	18.40	292.82	27.70	1.30
NWC	19.8	1000	−21.82	114.17	32.62	1.41
HWU	22.6	400	46.71	1.25	41.75	1.82
DHO	23.4	800	53.08	7.61	49.31	2.39
NAA	24.0	1000	44.65	292.72	53.23	2.83
NLM	25.2	233	46.37	261.67	56.00	3.25

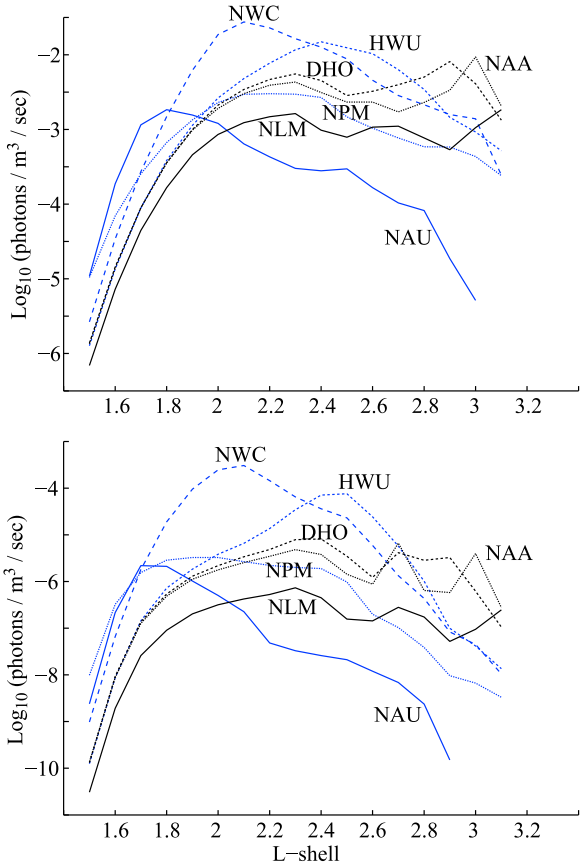

Figure 6. Photon volume emission rates in the N_2 1 P band system versus L for existing ground-based VLF transmitters for (top) square and (bottom) sine pitch angle distributions.

[25] Figure 7 shows the precipitated flux in energy units, for a transmitter at 35° magnetic latitude, with transmitted frequency of 20 kHz and power of 1 MW. The energy flux for electrons greater than a particular E_{min} for a range of E_{min} is shown. The topmost curve shows the energy due to all precipitating electrons with energies $E > 1$ keV; all other curves can be considered a subset of that curve. Similar curves for E_{min} = 300 eV, 100 eV, or even less show negligible difference compared to the E_{min} = 1 keV curve; this means that very little energy flux is contributed by electrons below 1 keV. However, while this is true for this 35° latitude transmitter, lower-energy electrons do result in a small peak at high L shells. These low-energy electrons are responsible for the emission peak at high L shells for NAA, NLM, and DHO in Figure 6.

[26] Figure 8 compares the effects of different transmitter and plasma parameters on the resulting optical emission rates. Each curve plots the peak volume emission rate in altitude along the magnetic meridian, as shown in Figure 6 and the discussion thereof. For the most part, these results are consistent with those found by *Kulkarni et al.* [2008]; as a result we provide a brief synopsis here. In each case, the control parameters are transmitter power and frequency of 1 MW and 20 kHz, magnetic latitude of 35°, a square pitch angle distribution, and a quiet plasmasphere, the latter two of which are shown in Figure 1.

[27] Figure 8a shows the peak optical emissions with varying transmitter frequency. We find that the emission rates are highest for the lowest transmitter frequency. This is identical to the results of *Kulkarni et al.* [2008]. Similarly, our results agree with *Kulkarni et al.* [2008] in that the highest emission rates are found for $\lambda = 35°$ (Figure 8b). However, in our results, there are significant peaks at higher latitudes due to precipitation of lower-energy (<100 keV) electrons. Third, Figure 8d shows that the volume emission rates increase almost linearly with transmitter power. Finally, Figure 8c shows that the plasmasphere conditions (quiet versus disturbed) do not play a significant role in the resulting optical signature, but the pitch angle distribution plays the most dominant role. As in Figure 6, the peak emission rates vary by almost 2 orders of magnitude between the extremes of the pitch angle distribution. This is a logical result since in the case of the sine pitch angle distribution, there are simply far fewer electrons near the loss cone angle, so fewer are scattered into the loss cone by the injected whistler mode waves.

[28] Given these results, we can see that the NWC transmitter (1 MW at 19.8 kHz, $\lambda = 32.62°$) is nearly ideal for precipitating energetic electrons from the radiation belts and optimizing the optical signature. As such it is no surprise that NWC creates the strongest optical signals in Figure 6. Doubling the transmitter power would, at best, double the peak optical signal from 50 mR to 100 mR, while variations in other parameters would make negligible improvements except perhaps lowering the transmitted frequency. Furthermore, we note that this 50 mR peak intensity results from a best-case pitch angle distribution (i.e., a square distribution); as such this is an upper limit on the peak intensity resulting from the NWC transmitter.

4. Implications for Experimental Detection

[29] Optical detection of transmitter-induced precipitation is very appealing as a diagnostic of the effects of ground-based transmitters on the radiation belt populations. Our

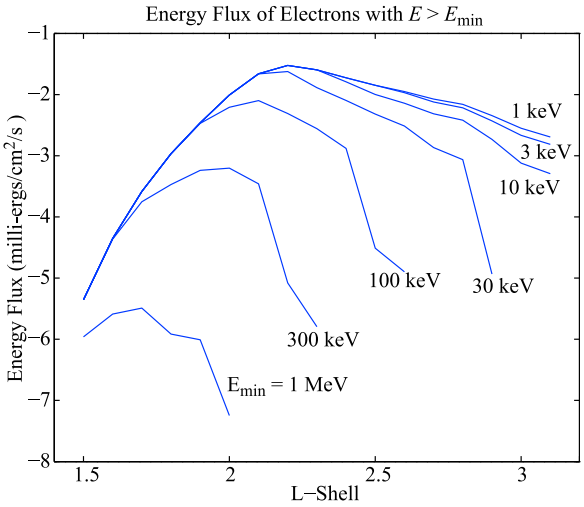

Figure 7. Precipitated energy flux versus L for the NWC transmitter (square pitch angle distribution). Each curve shows the precipitated energy flux due to electrons with energies above E_{min}.

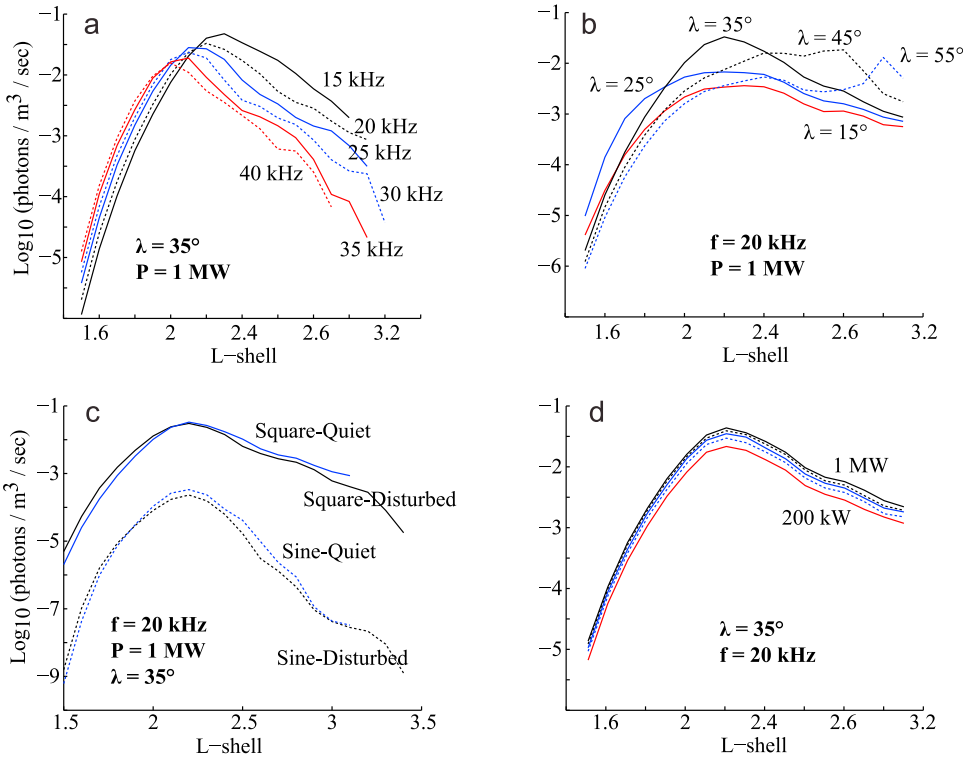

Figure 8. Variations in the N_2 1 P photon volume emission rates with (a) transmitter frequency, (b) transmitter geomagnetic latitude, (c) distribution type, and (d) transmitter power.

calculations in section 3 have shown that the highest optical signature we can expect is ~50 mR in the N_2 1 P bands and somewhat less in the N_2^+ 1 N bands and the O(^1S) 5577 Å line. Here we will investigate whether or not this small signal is detectable.

4.1. SNR Estimate

[30] For the sake of detectability arguments, we will consider the 5577 Å green line and the dominant 4278 Å line of the N_2^+ 1 N system and use an average intensity of 10 mR. The 6300 Å line is weak, and its O(^1D) state has an ~100 s lifetime (quenched to ~5–10 s at *D* and *E* region altitudes), hindering the sequential on-off experiment technique, and the N_2 1 P system is very broadband, so that any particular emission line will have only a small fraction ofthe total 50 mR.

[31] The detectability of these emissions is limited by the background sky brightness at night. The night sky background intensity, including both starlight and airglow emissions, varies between ~2 and ~5 R Å^{-1} over the broad wavelength range of 5000–6500 Å [*Shefov*, 1959]. In the blue and red regions, this background is somewhat lower and less than 1 R Å^{-1}. However, the natural airglow emissions in the green line, for example, average about 250 R [*Chamberlain*, 1995, section 12.3], which is added to the 10 mR signal we wish to detect. At 4278 Å the airglow is far less prominent and generally less than 1 R Å^{-1} [*Rees*, 1989, Figure 7.2.1], so we will assume a worst-case background of 1 R Å^{-1} from above.

[32] The best narrowband filters on the market have bandwidths of ~12 Å. Integrating in our two emissions, this yields an airglow signal of 12 R in the 4278 Å channel and (250 + 12 × 5) = 310 R in the 5577 Å channel. We can compute a system sensitivity as follows: 1 R (10^6 photons cm^{-2} s^{-1} (4π sr)$^{-1}$) into an optical system with 10 cm diameter and 10° × 10° field of view (0.008 sr) yields 1.6 × 10^6 photons s^{-1}. As an example detector, the Hamamatsu R5900U series of photomultiplier tubes has a quantum efficiency of ~0.4, a dark current at the anode of ~1 nA, and a gain of 10^6; this yields a cathode current of 50 fA per rayleigh. If we use this sensitivity in our optical system, the shot noise due to this background signal of I_{sky} = 15.5 pA is given by

$$I_{s,\mathrm{sky}} = \sqrt{2qI_{\mathrm{sky}}B}, \tag{3}$$

where B is the bandwidth of the recording system and q is the electron charge. Note that this signal is 15.5 μA at the anode, and as such the shot noise will dominate the dark or thermal noise. If we assume a sampling interval of 100 ms or a bandwidth of 10 Hz, then $I_{s,\mathrm{sky}}$ = 7.0 fA for the 5577 Å channel; this is to be compared to our signal of 10 mR, measured as 0.5 fA. This yields an SNR of ~0.07, so our signal is not likely to be detectable. Even worse, if we assume a sine pitch angle distribution, the peak intensity is only 0.1 mR, resulting in a signal current 100 times smaller and an SNR of 0.0007, making detection impossible. Note that the 4278 Å line has only an ~60 R background intensity, resulting in a shot noise of 3.1 fA and an SNR of ~0.16 for the square pitch angle distribution.

[33] Note that factors such as atmospheric absorption (which is especially significant at 4278 Å), filter transmis-

sion, and other system efficiencies will affect the signal as well as the background and the associated noise. These will affect the resulting SNR as well, decreasing it by up to a factor of 2.

4.2. Experimental Attempts

[34] Experimental attempts to measure these optical signatures have been undertaken by Stanford University since 2006. A multianode photometer array known as Photometric Imaging of Precipitation of Electron Radiation (PIPER) [*Marshall et al.*, 2008] is currently installed at the Gingin Observatory in Western Australia, as shown in Figure 5, and is pointed at the peak of the emission region in Figure 5 (bottom). Two pairs of Hamamatsu R5900U photomultiplier tubes are arranged with 10 nm (100 Å) bandwidth filters at 5577 Å and 4278 Å. Unfortunately, these wide-bandwidth filters add an appreciable amount of noise, increasing the background current to 37.5 pA and the shot noise to 10 fA and reducing the SNR to ~0.05 (for the square pitch angle distribution). Unsurprisingly, no obvious signature has yet been detected. A similar system is installed at Wallops Island, Virginia, United States, monitoring the precipitation signature due to the NAA transmitter.

[35] To improve the detectability of the optical signal, we conduct an experiment with the VLF transmitters wherein the transmitter is keyed on and off every 2 s, as described by *Inan et al.* [2007]. As the transmitter is turned on and off, the precipitation signal should also appear and disappear, with latency of ~1 s due to the propagation time of the injected whistler waves. If this pattern is repeated over 30 min, this yields 900 periods, increasing the SNR by a factor of $\sqrt{900} = 30$ to a best-case SNR of 2.1 for the 5577 Å line and 4.8 for the 4278 Å emission; these SNRs should now make the signal detectable (noting again that a sine pitch angle distribution will decrease these SNRs by a factor of 100). This keying experiment has been conducted a number of times at the NAA transmitter in 2008 and 2009, without successful signal detection. NWC keying experiments are expected to begin in late 2010.

4.3. Implication for LEP Events

[36] In this paper we have focused entirely on the optical signature of ground-based VLF transmitters; however, similar calculations can be made for LEP events. While we leave detailed calculations to future work, estimates can be made on the basis of existing results. Using a similar modeling technique, *Peter and Inan* [2007] report a peak precipitated energy flux of ~10 milliergs cm^{-2} s^{-1} for two lightning discharges with peak currents of +133 and −155 kA. This is ~3–4 orders of magnitude higher than our results for NWC (Figure 3). If we assume that the optical signature increases in proportion to the precipitated flux, this yields an optical intensity at the peak of ~50–500 R for the square pitch angle distribution, which is easily detectable in a single event; even the 0.5–5 R for the sine pitch angle distribution should be detectable.

[37] Future modeling work will be required, however, since the assumption that the optical intensity varies linearly with precipitated flux is far from accurate. Nonetheless, optical signatures of LEP events may yield important information about the precipitated fluxes and the state of the radiation belts during each event. Experimental attempts to measure these optical signatures are currently ongoing, and results are forthcoming.

5. Summary

[38] We have made estimates of the optical signatures due to energetic electron precipitation caused by ground-based VLF transmitters. These estimates involve a four-step procedure. First, we use a ray tracing and precipitation code developed by *Inan and Bell* [1977] to estimate the precipitated fluxes caused by ground-based transmitters with particular frequency, power, and location. Next, the precipitated flux is input into a Monte Carlo code to estimate the new ionization produced as a function of altitude. This new ionization is then used to compute optical emission rates, which are finally integrated to a camera view to determine the Rayleigh intensity.

[39] These calculations were conducted for seven existing ground-based transmitters, listed in Table 2, as well as for a variety of parameters to evaluate their individual effects. We find the following conclusions: (1) the lower the transmitter frequency, the more electrons are precipitated, and thus, an increase in optical emissions will result; (2) the optical signature is strongest for a transmitter at ~35° magnetic latitude; (3) the peak intensity in the optical signature increases almost linearly with transmitted power; (4) the optical signature is 2 orders of magnitude stronger for a square pitch angle distribution compared to a sine distribution; and (5) the quiet versus disturbed plasmasphere conditions have little effect on results. This latter result is due to the fact that VLF transmitter frequencies, which are always above 10 kHz, do not propagate beyond $L \simeq 3$ [*Kulkarni et al.*, 2008], and under disturbed or quiet conditions this inner part of the plasmasphere changes little.

[40] On the basis of the above parameters, we find that the NWC transmitter is nearly ideally placed for this purpose. However, the resulting optical signatures have peak intensities in the various observable bands 10–50 mR for a square pitch angle distribution. This can be compared to heater-induced artificial airglow, which is typically ~50 R in the 5577 Å green line but which is very easily detected with even 100 Å bandwidth filters. Our SNR calculations show that this 10–50 mR is unlikely to be detectable on top of the background airglow, with an SNR of ~0.07, but this SNR could increase to ~2.1 with 30 min of repeated experiments.

[41] **Acknowledgments.** This paper was supported by ONR grant N00014-06-1-1036.

[42] Robert Lysak thanks Anatoly V. Streltsov and Jean Lilensten for their assistance in evaluating this paper.

References

Abel, B., and R. M. Thorne (1998), Electron scattering loss in Earth's inner magnetosphere: 1. Dominant physical processes, *J. Geophys. Res.*, *103*(A2), 2385–2396.

Baker, D., G. M. Mason, O. Figueroa, G. Colon, J. G. Watzin, and R. M. Aleman (1993), An overview of the Solar, Anomalous, and Magnetospheric Particle Explorer (SAMPEX) mission, *IEEE Trans. Geosci. Remote Sens.*, *31*, 531–541.

Bell, T. F., V. P. Pasko, and U. S. Inan (1995), Runaway electrons as a source of red sprites in the mesosphere, *Geophys. Res. Lett.*, *22*(16), 2127–2130.

Bethe, H. A., and J. Ashkin (1953), *Experimental Nuclear Physics*, vol. 1, *Passage of Radiation Through Matter*, edited by E. Segre, John Wiley, New York.

Bortnik, J., U. S. Inan, and T. F. Bell (2006a), Temporal signatures of radiation belt electron precipitation induced by lightning-generated MR whistler waves: 1. Methodology, *J. Geophys. Res.*, *111*, A02204, doi:10.1029/2005JA011182.

Bortnik, J., U. S. Inan, and T. F. Bell (2006b), Temporal signatures of radiation belt electron precipitation induced by lightning-generated MR whistler waves: 2. Global signatures, *J. Geophys. Res.*, *111*, A02205, doi:10.1029/2005JA011398.

Cairó, L., and F. Lefeuvre (1986), Localization of sources of ELF/VLF hiss observed in the magnetosphere: Three-dimensional ray tracing, *J. Geophys. Res.*, *91*(A4), 4352–4364.

Carpenter, D. L., and R. R. Anderson (1992), An ISEE/whistler model of equatorial electron density in the magnetosphere, *J. Geophys. Res.*, *97*(A2), 1097–1108.

Chamberlain, J. W. (1995), *Physics of the Aurora and Airglow*, AGU, Washington, D. C.

Helliwell, R. A. (1965), *Whistlers and Related Ionospheric Phenomena*, Stanford Univ. Press, Stanford, Calif.

Helliwell, R. A., J. P. Katsufrakis, and M. Trimpi (1973), Whistler-induced amplitude perturbation in VLF propagation, *J. Geophys. Res.*, *78*(22), 4679–4688.

Inan, U. S., and T. F. Bell (1977), The plasmapause as a VLF wave guide, *J. Geophys. Res.*, *82*(19), 2818–2827.

Inan, U. S., M. Golkowski, M. K. Casey, R. C. Moore, W. Peter, P. Kulkarni, P. Kossey, E. Kennedy, S. Meth, and P. Smit (2007), Subionospheric VLF observations of transmitter-induced precipitation of inner radiation belt electrons, *Geophys. Res. Lett.*, *34*, L02106, doi:10.1029/2006GL028494.

Kulkarni, P., U. S. Inan, T. F. Bell, and J. Bortnik (2008), Precipitation signatures of ground-based VLF transmitters, *J. Geophys. Res.*, *113*, A07214, doi:10.1029/2007JA012569.

Lehtinen, N. G., T. F. Bell, V. P. Pasko, and U. S. Inan (1997), A two-dimensional model of runaway electron beams driven by quasi-electrostatic thundercloud fields, *Geophys. Res. Lett.*, *24*(21), 2639–2642.

Lehtinen, N. G., T. F. Bell, and U. S. Inan (1999), Monte Carlo simulation of runaway MeV electron breakdown with application to red sprites and terrestrial gamma ray flashes, *J. Geophys. Res.*, *104*(A11), 24,699–24,712.

Marshall, R. A., R. T. Newsome, and U. S. Inan (2008), Fast photometric imaging using orthogonal linear arrays, *IEEE Trans. Geosci. Remote Sens.*, *46*, 3885–3893, doi:10.1109/TGRS.2008.2000824.

Moss, G. D., V. P. Pasko, N. Liu, and G. Veronis (2006), Monte Carlo model for analysis of thermal runaway electrons in streamer tips in transient luminous events and streamer zones of lightning leaders, *J. Geophys. Res.*, *111*, A02307, doi:10.1029/2005JA011350.

Parrot, M. (Ed.) (2006), First results of the DEMETER micro-satellite, *Planet. Space Sci.*, *54*(5), 148 pp.

Peter, W. B., and U. S. Inan (2007), A quantitative comparison of lightning-induced electron precipitation and VLF signal perturbations, *J. Geophys. Res.*, *112*, A12212, doi:10.1029/2006JA012165.

Rees, M. H. (1989), *Physics and Chemistry of the Upper Atmosphere*, Cambridge Univ. Press, Cambridge, U. K.

Rees, M. H. (1992), Auroral energy deposition rate, *Planet. Space Sci.*, *40*(2–3), 299–313.

Sauvaud, J.-A., R. Maggiolo, C. Jacquey, M. Parrot, J.-J. Berthelier, R. J. Gamble, and C. J. Rodger (2008), Radiation belt electron precipitation due to VLF transmitters: Satellite observations, *Geophys. Res. Lett.*, *35*, L09101, doi:10.1029/2008GL033194.

Shefov, N. N. (1959), Intensities of some twilight and night airglow emissions, in *Spectral, Electrophotochemical, and Radar Researches of Aurorae and Airglow*, vol. 1, pp. 25–29, Acad. of Sci., Moscow.

Vallance Jones, A. (1974), *Aurora*, D. Reidel, Dordrecht, Netherlands.

U. S. Inan, N. Lavassar, N. G. Lehtinen, and R. T. Newsome, Space, Telecommunications, and Radioscience Laboratory, Stanford University, 350 Serra Mall, Rm. 306, Stanford, CA 94305, USA.

R. A. Marshall, Center for Space Physics, Boston University, 725 Commonwealth Ave., Boston, MA 02115, USA. (robertm@bu.edu)